Effect of undercut on the resonant behaviour of silicon nitride cantilevers

2009 J. Micromech. Microeng. 19 035003

(http://iopscience.iop.org/0960-1317/19/3/035003)

J. Micromech. Microeng. **19** (2009) 035003 (8pp) doi:10.1088/0960-1317/19/3/035003

Effect of undercut on the resonant behaviour of silicon nitride cantilevers

K Babaei Gavan[1], E W J M van der Drift, W J Venstra, M R Zuiddam and H S J van der Zant

Kavli Institute of Nanoscience, Delft University of Technology, Lorentzweg 1, 2628 CJ Delft, The Netherlands

E-mail: k.babaeigavan@tudelft.nl

Received 28 June 2008, in final form 11 November 2008
Published 30 January 2009
Online at stacks.iop.org/JMM/19/035003

Abstract

We present a systematic investigation of the dynamic properties of silicon nitride cantilevers in air. The thermal noise spectra of cantilevers have been measured using a home-made optical deflection setup. Torsional and flexural resonances up to the seventh mode are observed. The dependence of resonance frequencies on the dimensions and mode number is studied in detail. It is found that undercut increases the effective length of the cantilever by a value ΔL, which depends on the undercut distance and the resonance mode shape, but not on the cantilever length. Finite element modelling confirms these experimental findings. A simple model is suggested for the shape of the undercut region, which agrees well with experimental findings. Using this model, the undercut cantilever can be approximated by a stepped beam, where the clamp distance depends on the underetch duration and the mode shape.

(Some figures in this article are in colour only in the electronic version)

1. Introduction

Cantilever systems in the micro- and nanometer regimes have attracted great interest because of their wide range of sensor applications. Examples, both in fundamental and industrial areas, include Casimir force detection [1], material properties analysis [2, 3], magnetic resonance force microscopy (MRFM) [4] and extremely sensitive mass sensors [5–7]. Using the first natural frequency of the cantilevers for detection [8, 9], the mass sensitivity can be in the order of 10^{-19} g $(\mathrm{Hz})^{-1/2}$ which is suitable for single virus detection. Interest in higher modes is raised as they potentially offer higher sensitivity [10, 11]. New measuring techniques are currently investigated to realize on-chip readout at resonance frequencies on the order of MHz up to the GHz range [12].

In practical applications, such as scanning probes and mass or stress sensors, often silicon nitride cantilevers are used, with dimensions in the range of ten to several hundreds of micrometers. The present work is a systematic investigation of the resonance frequency as a function of dimensions of such cantilevers in air. The undercut is explicitly taken into account [2, 3]. Flexural and torsional resonances have been measured up to the seventh mode using the thermal noise spectra. With the presented results, the resonance frequency can be predicted more accurately from the design. This is of great importance in the design of cantilever sensors (arrays) and in appropriate analysis of cantilever material properties [2]. The latter aspect is the more so important when size-dependent behaviour may enter the cantilever characteristics upon further miniaturization.

[1] Author to whom any correspondence should be addressed.

2. Fabrication

2.1. Fabrication of cantilevers with undercut

Cantilevers with undercut are fabricated from home-made Low-Pressure Chemical Vapour Deposited (LPCVD) silicon nitride [13] on silicon (1 0 0). The SiN_x thickness ranges from 74 to 850 nm. The cantilever length varies from 25 to 100 μm and the width from 8 to 17 μm. For patterning of the SiN_x layers a two-layer resist is used: HSQ e-beam resist (Fox-12, 200 nm) on top of the photoresist (HPR, 0.5–1.5 μm thickness, depending on the SiN_x thickness). The HPR layer serves as an extra dry etch mask while etching the SiN_x layer (see figure 1).

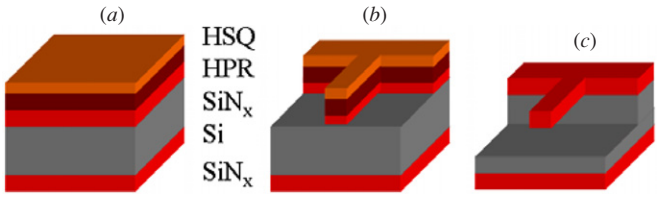

Figure 1. Cantilever fabrication process. (*a*) Overall layer stack. (*b*) After patterning of the silicon nitride layer. (*c*) Release of the cantilever structure by an isotropic dry etch process.

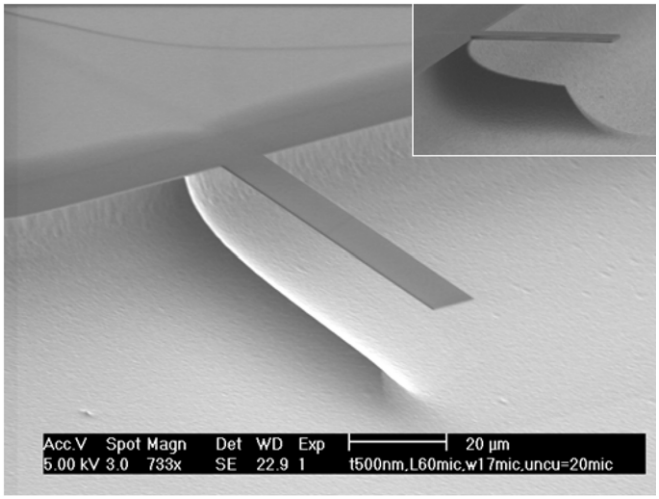

Figure 2. Scanning electron microscope (SEM) image of a silicon nitride cantilever. The base of the cantilever is underetched; the dark strip near the base of the cantilever indicates the undercut. The inset shows the anchoring in more detail: the short release etch time yields a protrusion which curves towards the cantilever.

The HSQ layer is patterned using an electron beam pattern generator (Leica 5000$^+$). After development, two anisotropic dry etch steps follow to etch through the HPR and SiN_x layers as shown in figure 1(*a*). First, HPR is anisotropically etched by a low-pressure O_2 reactive ion etching (RIE) plasma (LH Z400 system at 20 sccm, 0.3 μbar, 40 W), and next the SiN_x by a low-pressure O_2/CHF_3 (2.5 sccm, 50 sccm, 10 μbar) RIE plasma at 50 W. Then, a selective isotropic dry etch step follows with an SF_6/O_2 inductively coupled plasma (Alcatel AMS100) to release the cantilevers (figure 1(*c*)). In this final step the undercut is introduced at the base of the cantilevers, as shown in figure 2.

2.2. *Fabrication of cantilevers without undercut*

Cantilevers without undercut are fabricated as well. In this case, double-side polished silicon (1 0 0) wafers coated with LPCVD silicon nitride on both sides are used. Square windows are made in the nitride on the back side of the wafer, through which the Si is wet etched till a SiN_x membrane results at the front side. A KOH solution is used (H_2O:KOH = 25 ml:9 g; etch rate 1 μm min^{-1}) creating the well-known pyramidal features according to the silicon (1 1 1) facets.

In a second lithography step, the cantilever pattern is defined in the silicon nitride membrane, which has a thickness

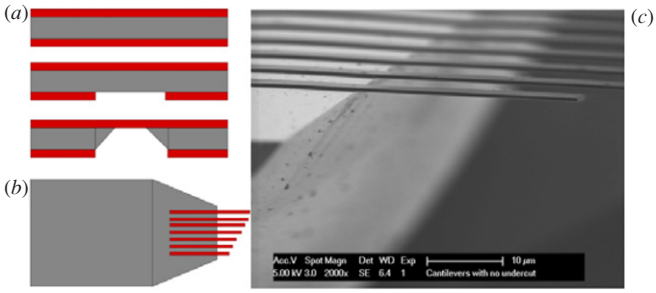

Figure 3. Fabrication of cantilevers without undercut. (*a*) Schematic side view of the membrane fabrication steps. (*b*) Schematic top view after the cantilever release with the nitride stripes extending from the base to free space, without any undercut. (*c*) SEM image of the SiN_x cantilevers.

of 500 nm. The membrane is spin coated with HPR (900 nm) photoresist and on top HSQ (Fox-12, 200 nm) e-beam resist. After e-beam patterning and development the cantilevers are released using the same sequence of O_2 and O_2/CHF_3 plasma steps indicated for the undercut devices. The schematics of the fabrication process are shown in figures 3(*a*)–(*b*). An example of fabricated cantilevers without undercut is shown in figure 3(*c*).

3. Measurement setup

The resonance behaviour of the cantilevers is measured in a home-made optical laser deflection setup operating in atmospheric environment. Figure 4 depicts the configuration of the setup. The deflection of the cantilevers due to thermal noise is probed by a 658 nm (New-Focus) laser diode. The output signal, the voltage difference generated by the reflected light focused on a two-segment diode, is measured with a spectrum analyser to obtain thermal noise spectra. The laser spot is typically positioned at the end of the cantilever with a spot diameter of 6 μm and a power of a few mW. The electronic bandwidth of the setup is 5 MHz and its sensitivity is estimated to be about 1 pm (Hz)$^{-1/2}$. We have reduced the laser power by a factor of 2 and found that the noise spectra are not affected. Therefore, the measured spectra are attributed to thermal fluctuations and not to excitations induced by the laser.

Thermal noise spectra are measured for a large number of cantilevers with varying length (L), thickness (t) and width (w). Figure 5 shows three spectra of a 74 nm thick cantilever. Flexural modes (upper panel: modes 2–6 are clearly visible in this case) and torsional modes (middle panel: modes 1–5) can be measured independently [14] by rotating the cantilever with respect to the incoming laser beam. The insets in figure 5 schematically show the movement of the reflected laser beam on the two-segment diode. Flexural movements of the cantilever result in horizontal beam deflections (top figure 5), which can be detected since the laser generates a periodic signal on the two-segmented photodiode. In this configuration, the detector is insensitive to the vertical beam deflections which represent the torsional movements. In the middle figure 5 the sample has been rotated by 90°. Now

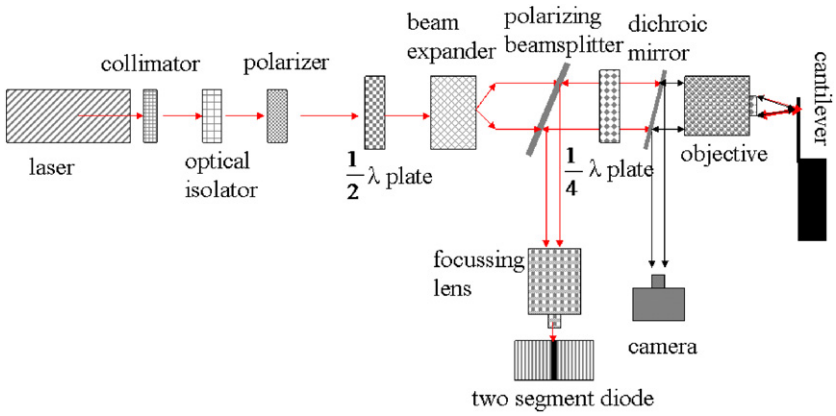

Figure 4. Schematic of the home-made optical deflection setup.

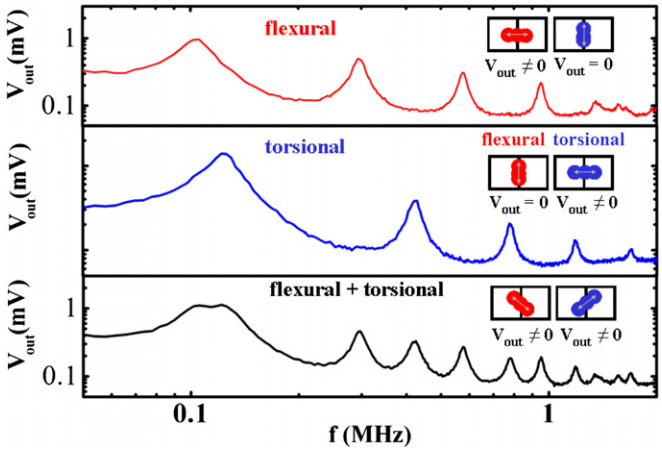

Figure 5. Thermal noise spectra of a SiN_x cantilever with dimensions $w \times L \times t = 17 \times 60 \times 0.074\ \mu m^3$. Distinction between the torsional and flexural modes is obtained by rotating the cantilevers by 90°. With a rotation of 45° both flexural and torsional modes are visible (lower panel). The insets illustrate the motion of the reflected laser beam on the segmented diode.

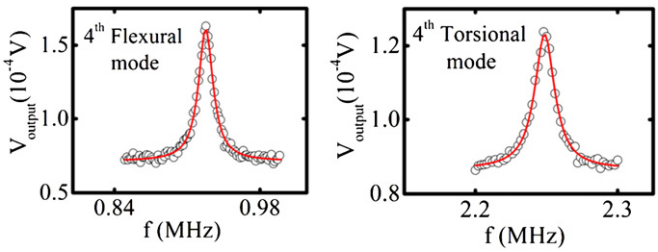

Figure 6. Zoom-in on the fourth torsional and flexural modes; red lines are Lorentzian fits through the data defining the position of the resonance and its Q factor.

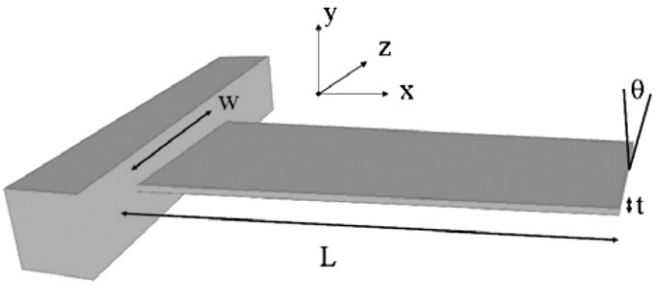

Figure 7. Schematic view of a uniform beam with rectangular cross section with nominal length L, width w and thickness t and $w \gg t$. The angle θ denotes the rotation around the x-axis.

torsional movements can be detected and for the flexural modes the output voltage equals zero. When the sample is placed at 45°, the reflections from the flexural and torsional modes make an oblique movement and both modes are detected at the same time. The independent identification of the modes is an advantage of measuring thermal noise spectra; measurements on actuated cantilevers generally show the two types of modes at the same time [15].

The resonance frequency and the Q-factor of the resonances are determined from Lorentzian fits (red lines) through the data, as is illustrated in figure 6 for the fourth torsional and flexural modes. In the next sections, we will discuss in more detail the dependence of the resonant frequencies on the cantilever geometry.

4. Flexural modes

The equation of motion for the flexural vibration modes in vacuum (quality factor $Q \gg 1$) and its solutions can be found in the text books [16, 17] and is briefly summarized here for convenience. We will adopt the notation shown in figure 7 and note that the starting point for the calculation of the resonance frequencies is the Euler–Bernoulli beam equation:

$$EI\frac{\partial^4 y}{\partial x^4} + \rho A\frac{\partial^2 y}{\partial t^2} = 0, \tag{1}$$

where E is the Young's modulus, I is the area moment of inertia, ρ is the mass density, and A is the cross-sectional area.

The harmonic vibration solution can be found using the method of separation of variables with $Y(x,t) = u(x)\,e^{i\omega t}$, which simplifies (1) for the spatial solution to

$$\frac{d^4u(x)}{dx^4} - k^4u(x) = 0, \tag{2}$$

where

$$k^4 = \frac{\rho A(2\pi f)^2}{EI} \tag{3}$$

Table 1. The frequencies and Q-factors of the first seven flexural modes of a cantilever with dimensions ($w \times L \times t = 17 \times 100 \times 0.2\ \mu m^3$). The theoretical and experimental f_n/f_1 are in good agreement. The error in all measurements of f_n was within ± 10 Hz.

N	f_n (MHz)	Q-factor	f_n/f_1 (theory)	f_n/f_1 (exp)
1	0.032	2.2	1	1
2	0.21	13.3	6.267	6.51
3	0.59	35.2	17.548	18.29
4	1.26	66.2	34.389	35.87
5	1.90	92.8	56.843	59.15
6	2.80	124	84.914	87.93
7	3.90	∼100	118.599	121.54

is the characteristic parameter of the system and f is the resonance frequency. The general solution to (2) is given by

$$u(x) = a_1 \sin(kx) + a_2 \cos(kx) + a_3 \sinh(kx) + a_4 \cosh(kx). \tag{4}$$

For cantilevers, the boundary conditions are

$$u(0) = \frac{\mathrm{d}u(0)}{\mathrm{d}x} = \frac{\mathrm{d}^2u(L)}{\mathrm{d}x^2} = \frac{\mathrm{d}^3u(L)}{\mathrm{d}x^3} = 0.$$

A non-trivial solution for the prefactors in (4), leads to the characteristic equation

$$1 + \cos(k_n L)\cosh(k_n L) = 0. \tag{5}$$

The solutions $\{\alpha_n = k_n L$ with $n = 1, 2 \ldots\}$ of (5) give the wave numbers k_n of a set of flexural vibration modes, where n is the mode number. Combining the solutions of (5) with (3), one finds the resonance frequency of the cantilevers in terms of the dimensions and the material properties:

$$f_n = \frac{\alpha_n^2}{2\pi\sqrt{12}} \frac{t}{L^2} \sqrt{\frac{E}{\rho}}, \tag{6}$$

where we have substituted $A = wt$ and $I = wt^3/12$.

For the first seven modes the mode-dependent α_n is given by 1.8751, 4.694, 7.855, 10.996, 14.1372, 17.2788 and 20.4204, respectively. With these numbers the ratio f_n/f_1 is calculated as shown in table 1. Equation (6) is to within a 2% error valid for rectangular cantilever plates (thin beams) with a small aspect ratio ($L/w > 1.5$) [18]. Experimental values determined from a 200 nm thick cantilever are given in the same table; they are in good agreement with the theoretical values. For other cantilevers we also find f_n/f_1 values that are close to those listed in table 1. We note that a slightly better agreement can be obtained if we correct the frequencies for the low Q-factors. In the harmonic approximation, the correction equals $(1–1/(4Q^2))^{-1/2}$ [19] and the ratios are then equal to 6.34, 17.81, 36.18, 57.29, 84.42 and 117.59, respectively.

To further test the applicability of the Euler–Bernoulli theory, we have measured the resonance frequencies as a function of length, thickness and width. Figure 8 shows the dependence of the fundamental resonance frequency f_1 versus L^{-2} in samples without undercut. The observed linear dependence is in agreement with (6). The dependence of f_1 on the thickness is shown in figure 9, for cantilevers with a fixed undercut. For a fixed cantilever length, a linear behaviour is observed, in accordance with (6).

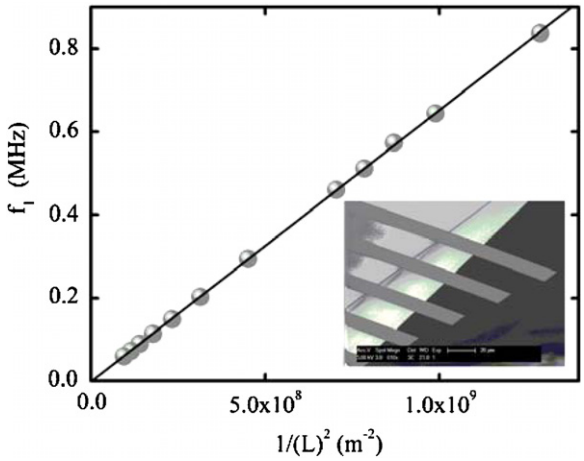

Figure 8. Resonance frequency of the first mode versus $1/L^2$ showing the expected linear dependence of (6). These measurements were performed on cantilevers without undercut as shown in the inset SEM image. Cantilever thickness and width are 500 nm and 17 μm, respectively. The length varies from 20 to 100 μm.

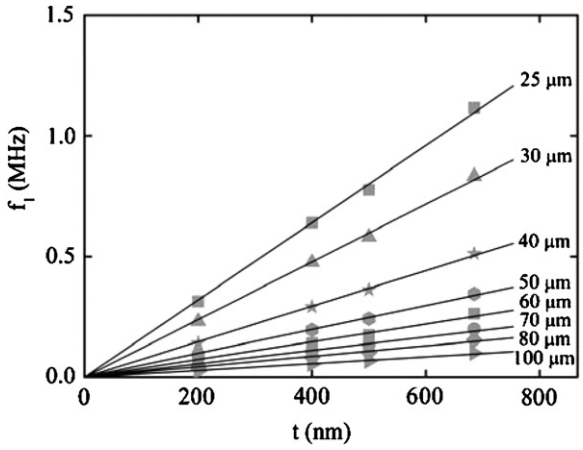

Figure 9. Fundamental resonance frequency versus thickness for different cantilever lengths, showing the expected linear dependence of (6).

5. Torsional modes

Apart from the flexural modes (the xy-plane) the cantilever also has other degrees of freedom. Vibration in the xz-plane is also possible although in practice the amplitudes of those modes are much smaller and more difficult to detect due to a higher stiffness ($I = tw^3/12$ instead of $I = wt^3/12$). Torsional modes refer to displacements due to rotation around the cantilever x-axis and the corresponding resonance frequencies of these modes are within our detection range. The equation of motion is given by [20]

$$T\frac{\partial^2\theta}{\partial x^2} - \rho I_p \frac{\partial^2\theta}{\partial t^2} = 0,$$

where T is the torsional stiffness, $\theta(x, t)$ is the angle of twist about the x-axis (figure 7), and I_p is the polar moment of inertia given by

$$I_p = I_y + I_z = \frac{wt^3}{12} + \frac{tw^3}{12}$$

for the cross section in the yz-plane. In practice, $t^3\, w \ll t\, w^3$ so that the first term can be neglected.

The torsional stiffness [21] $T = \eta G$ in which the shear modulus G is given by $G = E/2(1+\nu)$, with ν being Poisson's ratio. The factor η is dependent on the geometry of the cross section and will be discussed later. By the method of separation of variables [22]

$$\frac{\mathrm{d}^2\Theta(x)}{\mathrm{d}x^2} + \lambda_n^2\Theta(x) = 0, \qquad \text{with} \quad \lambda_n^2 = \frac{\rho I_p}{T}\,\omega^2. \tag{7}$$

The general solution to (7) is

$$\Theta(x) = b_1 \sin(\lambda_n x) + b_2 \cos(\lambda_n x),$$

with boundary conditions:

$$\Theta|_{x=0} = T\left.\frac{\partial\Theta}{\partial x}\right|_{x=L} = 0.$$

The latter term indicates that there is no torque applied at the free end of the cantilever and from this boundary condition one obtains the characteristic equation:

$$\cos(\lambda_n L) = 0, \qquad \text{with} \quad \lambda_n = \frac{(2n-1)\pi}{2L}$$

so that

$$f_n = \frac{2n-1}{4L}\sqrt{\frac{\eta G}{\rho I_p}}.$$

The remaining problem is to find the value of η. When the cross section of the beam is considered to be an ellipse with the axis lengths equal to the width w and the thickness t of the cantilever, then $\eta = t^3 w/3$ and the resonance frequency in the absence of damping equals

$$f_n = \frac{2n-1}{2L}\frac{t}{w}\sqrt{\frac{G}{\rho}}. \tag{8}$$

For a narrow rectangular shaped beam, a better approximation is given by [23]

$$\eta \approx \frac{1}{3} w t^3 \left(1 - 0.630\frac{t}{w}\right).$$

For the beams in this study, the difference between these two approximations is less than 1% and we will use (8) to calculate the resonance frequencies for the torsional modes.

Figure 10 shows the resonance frequencies of the first torsional mode for a sample without undercut. The frequency versus reciprocal length does not show the expected linear dependence (8). An upward curvature is observed instead: shorter cantilevers have a higher resonance frequency than that expected from (8). This can be explained by taking into account the ratio L/w of the cantilever, according to the theory of Reissner and Stein [24]. With the measured Young's modulus obtained from the flexural modes (200 GPa for the cantilevers released by wet etching), and the Poisson's ratio of 0.22 from literature [25], we have calculated the torsional resonance frequencies predicted by this theory. As figure 10 shows, the data are in good agreement with this calculation.

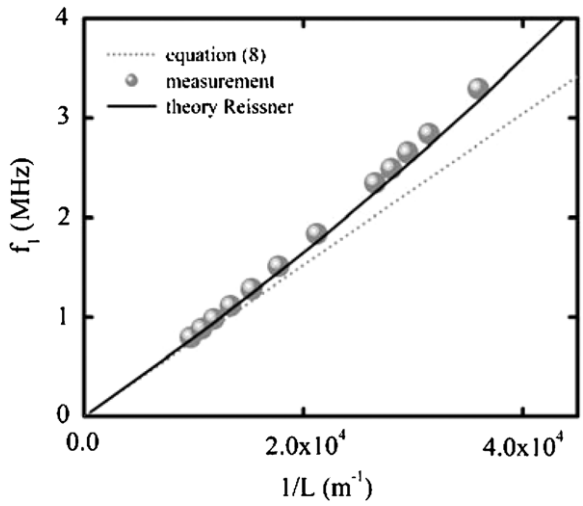

Figure 10. Resonance frequency of the first torsional mode versus the inverse of length, for cantilevers without undercut. Dotted line: solution according to (8). Solid black line: solution when the finite L/w ratio is taken into account. The cantilever width is 17 μm, and the thickness is 500 nm.

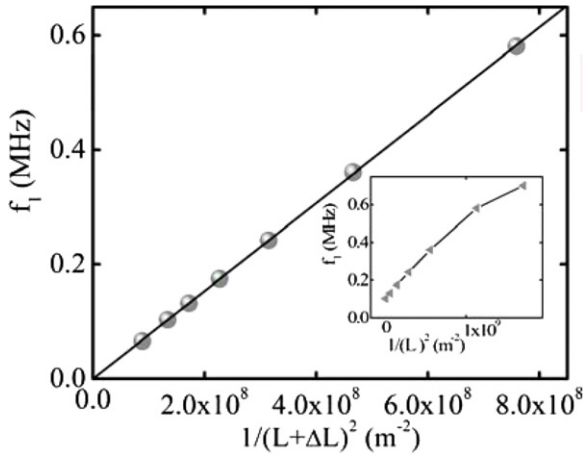

Figure 11. Fundamental resonance frequency of the flexural mode versus $1/(L+\Delta L)^2$. ΔL is a correction (6.7 μm in this case) to the nominal length L due to the underetch L_u (12.5 μm for this sample). Inset: f_1 versus $1/L^2$. Cantilever thickness and width are 500 nm and 17 μm, respectively.

6. The effects of undercut

6.1. Flexural modes

To investigate the effect of undercut on the cantilever resonance frequency, we now turn to the length dependence of modes in the samples with undercut. The inset of figure 11 shows the result. The undercut, which is 12.5 μm in this sample, leads to a deviation from the linear relation predicted by (6) and observed for devices without undercut in figure 8. The deviation from linearity is most pronounced for short cantilevers. Apparently, the base region near the anchoring point participates in the overall resonance behaviour of the cantilever. The effect of undercut can be included by adding a length ΔL to the nominal cantilever length [26–28], where ΔL is independent of the length of the cantilever. Thus

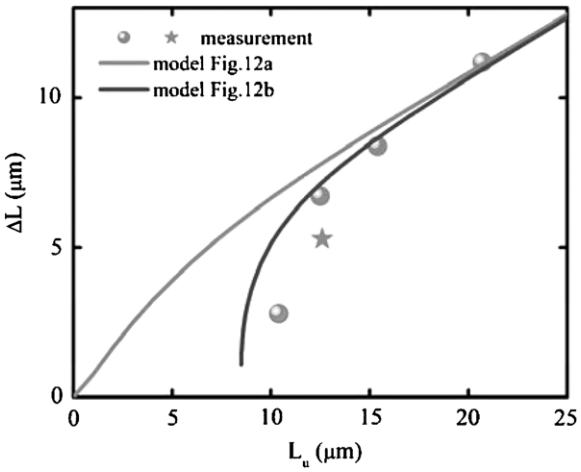

Figure 12. Correction ΔL to the nominal length as a function of the undercut length for the first flexural mode. •, four different batches of samples with a cantilever thickness of 500 nm; ⋆, one batch of samples with a cantilever thickness of 200 nm. Both errors in L_u and ΔL are well within the diameter of the circles. Drawn lines are the result of a finite-element simulation according to models schematically depicted in figure 13. Grey and black lines refer to undercut without (figure 13(*a*)) and with (figure 13(*b*)) protrusion.

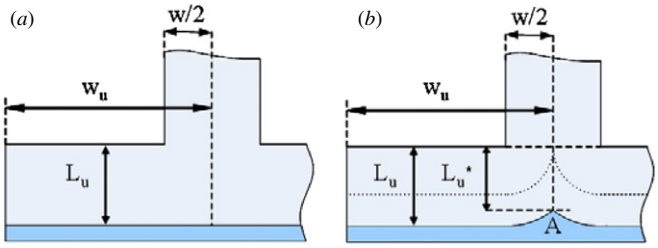

Figure 13. Schematic top view of the clamp region of a cantilever with underetch. (*a*) Idealized underetch with complete removal of substrate material over a length L_u, (*b*) more realistic underetch geometry with a protrusion due to partial removal of the substrate material over an effective length L_u^*. Dashed line refers to the contour for just sufficient underetch to release the cantilever beam over its full width.

the 'effective length' of the underetched cantilever is given by $L + \Delta L$. By performing a least-square fit (fit function: $f(x) = a/(L + \Delta L)^2$) through the resonance frequency data with ΔL and a as free parameters, ΔL was determined to be 6.7 μm for the data shown in figure 11. With the inclusion of ΔL, a linear relation between the resonance frequency f_1 and $1/(L + \Delta L)^2$ is obtained, as illustrated in figure 11.

A similar analysis has been performed on three other batches of samples with undercuts of 10.4 μm, 15.4 μm and 20.7 μm. The linear relation between f_1 and $1/(L + \Delta L)^2$ is restored for ΔL equal to 2.8, 8.4 and 11.2 μm, respectively. These fit values are plotted versus the experimental undercut distance L_u, as shown in figure 12 for the first resonance frequency (circles). The undercut distance, L_u, has been determined from SEM inspection.

For higher mode numbers, we also found a discrepancy between f_n and L^{-2}. Again, an effective length can be defined to restore the expected linear behaviour between the two parameters. The dependence of ΔL on the first three flexural modes has been investigated for 200 nm thick cantilevers and we find an increase of ΔL as the mode number increases: $\Delta L = 5.3$ μm for $n = 1$ (slightly smaller than the value for the 500 nm thick cantilevers; see figure 12), $\Delta L = 7.8$ μm for $n = 2$ and $\Delta L = 8.6$ μm for $n = 3$. Apparently, for the higher modes an increasing part of the base participates in the vibration.

To support the experimental findings a three-dimensional finite element simulation was carried out in ANSYS using 20 node structural solid elements (SOLID186 and SOLID95) and an element size of 1–5 μm. The underetched cantilever is modelled as a stepped beam as depicted in figure 13(*a*), and with a more realistic clamp which mimics the actual situation of an isotropic etching process when releasing the cantilevers (figure 13(*b*)). Released areas of cantilever and base regions are allowed to move freely. All translational and rotational degrees of freedom are set to zero throughout the cross section at the clamping regions where release is zero. As for input parameters the experimental value for the Young's modulus has been used (239 GPa) whereas the density (3100 kg m^{-3}) and Poisson's ratio (0.22) are taken from the literature [25]. The simulations show that indeed a ΔL can be defined and its values have been determined in the same way as in the experiments, i.e., by considering the frequency versus L^{-2} dependence. Note that the results shown are from simulations with $w_u > 10\,w$, where $2w_u$ is the total width of the simulated structure (see figure 13). In this limit, the calculated ΔL is independent of w_u. If w_u is smaller, the effective cantilever length increases since the structure becomes less stiff.

For the idealized underetch case (figure 13(*a*)), the grey line in figure 12 shows the calculated ΔL versus calculated underetch length L_u. As expected, the line crosses the origin: any undercut makes the effective cantilever length larger than the defined length. This behaviour is in contrast with the experimental data points which indicate a dependence with an intercept on the x-axis around 10 μm.

The black line in figure 12 shows the calculated ΔL versus underetch for the fundamental mode f_1 when the protrusion is explicitly taken into account. To model the protrusion, an isotropic etching process is taken at a constant etch rate k. The apex of the protruding tip, marked A, is positioned a distance L_u^* from the cantilever base (see figure 13(*b*)). The minimum underetch required to release the cantilever is half the cantilever width w. From the geometry, the position of the support is calculated as $L_u^* = \sqrt{(k\tau)^2 - (w/2)^2}$, where τ is the etching time. The etch rate of the apex is found by differentiating its position to the etch time:

$$\frac{\mathrm{d}L_u^*}{\mathrm{d}\tau} = \frac{k^2\tau}{\sqrt{(k\tau)^2 - (w/2)^2}} > k, \qquad \text{with} \quad k\tau > w/2. \tag{9}$$

The apex remains sharp, as is observed in the experiment. Note that just after the cantilever is released, when $k\tau \approx w/2$, the apex etch rate $\frac{\mathrm{d}L_u^*}{\mathrm{d}\tau}$ is high. In practice, this results in poor control over the undercut of the released cantilever right after release.

The model with protrusion (black line in figure 12) shows a much better agreement with the experimental data. For

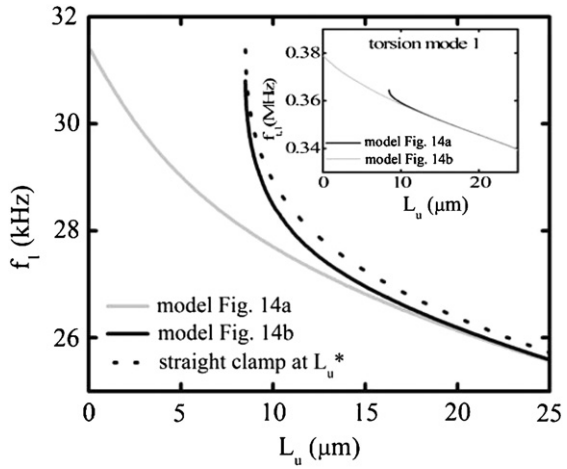

Figure 14. Resonance frequency as a function of undercut for the first flexural (main panel) and first torsional (inset) mode, calculated using the models of figure 13(*a*) (grey line) and figure 13(*b*) (black line). The cantilever dimensions are $w \times L \times t = 17 \times 100 \times 0.2\ \mu\text{m}^3$.

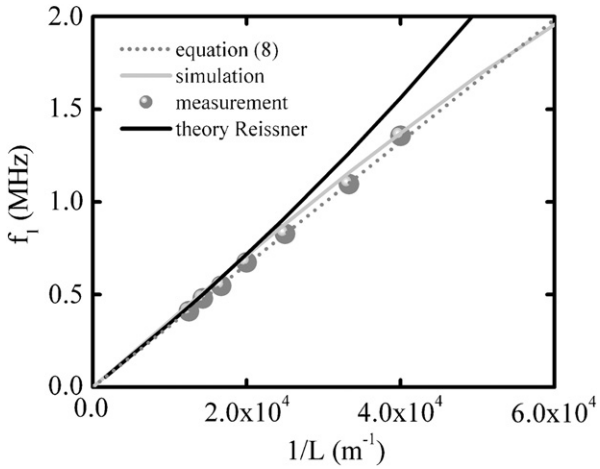

Figure 15. Torsional resonances as a function of the inverse length. The 200 nm thick cantilevers have an undercut of 10 μm. Also is shown the values according to the Reissner/Stein theory (black solid line) and the values (dotted line) calculated using (8).

low L_u, however, the model predicts slightly higher ΔL values compared to the measured ones. This discrepancy is attributed to a more complicated etch profile than that assumed in our 2D model. As can be seen in the inset of figure 2, the sharp underetch shape is slightly curving back towards the cantilever which makes the cantilever's effective length shorter than modelled. For large L_u, this effect becomes less pronounced, and the simulated and experimental values coincide. We also modelled the higher modes. As in the experiment, we find a slight increase of the ΔL values with increasing mode number.

Figure 14 shows a comparison between the calculated resonance frequencies of the first bending mode versus underetch for the two models. As expected, the effect of the protruding support vanishes when the undercut length $L_u > w$. For underetch lengths up to the cantilever width, the protrusion plays a significant role. For small undercuts ($L_u < 0.5\ w$) the cantilever length effectively becomes much shorter than L as only the outer tip of the cantilever is released. We note that for the description of the undercut on flexural modes, a reasonable approximation can be obtained by assuming a straight clamp at L_u^*, as shown by the dotted line in figure 14. Here, L_u^* can be calculated using (9). The underetch region is then simplified to a stepped beam geometry, which has been studied in the past [29].

6.2. Torsional modes

For torsional resonances the effect of the protrusion is expected to be less pronounced, as the support concentrates at the cantilever central length axis, which is a nodal line. The inset of figure 14 shows the dependence of the resonance frequency on L_u, simulated using the models in figures 13(*a*) and (*b*). In contrast to the bending modes, for the torsional modes the role of the protrusion is indeed insignificant: the base can be simplified as if it were clamped at L_u. This means that the stepped beam model of figure 13(*a*) can be applied. Note that it does not mean that the effective cantilever length increases by this amount, as we will show below.

Figure 15 shows the measured fundamental torsional resonance frequency versus the reciprocal length for 200 nm thick cantilevers with an undercut of 10 μm. Simulations (grey line) agree well with the experiments. The torsional frequencies according to Reissner and Stein theory, which takes into account the aspect ratio L/w [22], but not the undercut, are also plotted (black line). In this particular case, the effect of undercut is compensated by the decreasing L/w aspect ratio, and as a result (8) gives a good approximation to the data (dashed line).

As with the flexural modes, in the case of torsional modes the effective cantilever length is larger than the physical length. For the data in figure 15, we estimate a ΔL of 3.7 μm, which is different from the corresponding value of the flexural modes.

7. Summary and conclusions

We have studied the resonance behaviour of silicon nitride cantilevers in air, and compared the experimentally obtained results to existing beam and plate theories, and finite element simulations. Torsional and flexural modes can be distinguished in the thermal noise spectra by rotating the sample over 90°. For both types of vibrations, higher modes are observed. The flexural modes of cantilevers without undercut behave according to the Euler–Bernoulli theory. However, the presence of undercut results in a significant deviation from this theory. We show that a correction can be made to the nominal cantilever length to restore the relation between frequency and length. This correction is independent of the cantilever length, but varies with mode number. In the case of the torsional modes also a deviation due to the undercut has been observed, but different from the flexural mode observations. Finite-element simulations of the resonance frequency behaviour of the various modes are in good agreement with the experiments and support our findings.

Acknowledgments

We thank Dr Pereira from the Optics Research Group at Delft University of Technology and Dr Allard Katan from Interface Physics Group at Leiden University for their help in setting up the experiments. We thank the Dutch organization for Fundamental Research on Matter (FOM), NWO (VICI program) and NanoNed for financial support.

References

[1] Bressi G, Carugno G, Onofrio R and Ruoso G 2002 Measurement of the Casimir force between parallel metallic surfaces *Phys. Rev. Lett.* **88** 041804
[2] Sekaric L, Parpia L J M, Craighead H G, Feygelson T, Houston B H and Butler J E 2002 Nanomechanical resonant structures in nanocrystalline diamond *Appl. Phys. Lett.* **81** 4455–7
[3] Jenkins N E, DeFlores L P, Allen J, Ng T N, Garner S R, Kuehn S, Dawlaty J M and Marohn J A 2004 Batch fabrication and characterization of ultrasensitive cantilevers with submicron magnetic tips *J. Vac. Sci. Technol.* B **22** 909–15
[4] Rugar D, Budakian R, Mamin H J and Chui B W 2004 Single spin detection by magnetic resonance force microscopy *Nature* **430** 329–32
[5] Ekinci K L, Huang M H and Roukes M L 2004 Ultrasensitive nanoelectromechanical mass detection *Appl. Phys. Lett.* **84** 4469–71
[6] Yang Y T, Callegari C, Feng X L, Ekinci K L and Roukes M L 2006 Zeptogram-scale nanomechanical mass sensing *Nano. Lett.* **6** 583–6
[7] Jensen K, Kim K and Zettl A 2008 An atomic-resolution nanomechanical mass sensor *Nat. Nanotechnol.* **3** 533–7
[8] Illic B, Yang Y and Craighead H G 2004 Virus detection using nanoelectromechanical devices *Appl. Phys. Lett.* **85** 2604–6
[9] Gupta A K, Nair P R, Akin D, Ladisch M R, Broyles S, Alam M A and Bashir R 2006 Anomalous resonance in a nanomechanical biosensor *Proc. Natl. Acad. Sci. USA* **103** 13362–7
[10] Sharos L B, Raman A, Crittenden S and Reifenberger R 2004 Enhanced mass sensing using torsional and lateral resonances in microcantilevers *Appl. Phys. Lett.* **84** 4638–40
[11] Dohn S, Sandberg R, Svendsen W and Boisen A 2005 Enhanced functionality of cantilever based mass sensors using higher modes *Appl. Phys. Lett.* **86** 233501–3
[12] Li M, Tang H X and Roukes M L 2007 Ultra-sensitive NEMS-based cantilevers for sensing, scanned probe and very high-frequency applications *Nat. Nanotechnol.* **2** 114–20
[13] French P J, Sarro P M, Mallée R, Fakkeldij E J M and Wolffenbuttel R F 1997 Optimization of low-stress silicon nitride process for surface-micromachining applications *Sensors Actuators* A **58** 149–57
[14] Green C P, Lioe H, Mulvaney P and Sader J E 2004 Normal and torsional spring constants of atomic force microscope cantilevers *Rev. Sci. Instrum.* **75** 1988–96
[15] McFarland A W, Poggi M A, Bottomley L A and Colton J S 2005 Characterization of microcantilevers solely by frequency response acquisition *J. Micromech. Microeng.* **15** 785–91
[16] Sarid D 1991 *Scanning Force Microscopy* (Oxford: Oxford University Press)
[17] Timoshenko S P, Young D H and Weaver W 1974 *Vibration Problems in Engineering* 4th edn (New York: Wiley)
[18] Looker J R and Sader J E 2008 Flexural resonant frequencies of thin rectangular cantilever plates *J. Appl. Mech.* **75** 011007
[19] Giancoli D C 1989 *Physics for Scientists and Engineers with Modern Physics* 2nd edn (Englewood Cliffs, NJ: Prentice-Hall)
[20] Ginsberg J H 2001 *Mechanical and Structural Vibrations* (New York: Wiley)
[21] Timoshenko S P and Goodier J N 1970 *Theory of Elasticity* (New York: McGraw-Hill)
[22] Gorman D J 1975 *Free Vibration Analysis of Beams and Shafts* (New York: Wiley)
[23] Mendels D A, Lowe M, Cuenat A, Cain M G, Vallejo E, Ellis D and Mendels F 2006 Dynamic properties of AFM cantilevers and the calibration of their spring constants *J. Micromech. Microeng.* **16** 1720–33
[24] Reissner E and Stein M 1951 Torsion and transverse bending of cantilever plates *N.A.C.A. Technical Note 2369*
[25] Khan A, Philip J and Hess P 2004 Young's modulus of silicon nitride used in scanning force microscope cantilevers *J. Appl. Phys.* **95** 1667–72
[26] Cleland A N, Pophristic M and Ferguson I 2001 Single-crystal aluminum nitride nanomechanical resonators *Appl. Phys. Lett.* **79** 2070–2
[27] Yahiaoui R and Bosseboeuf A 2004 On thermal and mechanical simulations and experiments in micro-electronics and micro-systems *5th Int. Conf. EuroSim E.* 377–84
[28] Bhattacharya S and Bhattacharya E 2007 Electrical measurement of undercut in surface micromachined structures *International Workshop on the Physics of Semiconductor Devices (IWPSD) Bombay 2007* 702–5
[29] Jang S K and Bert C W 1989 Free vibration of stepped beams: exact and numerical solutions *J. Sound Vib.* **130** 342–6